A Stilbene-Strontium Iodide Based Radioxenon Detection System for Monitoring Nuclear Explosions

Harish R. Gadey[a], Abi T. Farsoni[b], Steven A. Czyz[c]*

*Corresponding Author: harish.gadey@pnnl.gov

[a]Pacific Northwest National Laboratory, 902 Battelle Blvd, Richland, WA 99354

[b]Oregon State University, 3451 SW Jefferson Way Corvallis, OR 97331

[c]Lawrence Livermore National Laboratory, 7000 East Ave, Livermore, CA 94550

Abstract

Atmospheric measurement of noble gases has been extensively used for monitoring nuclear weapon explosions for many years. The ratios of four xenon isotopes of interest (^{131m}Xe, ^{133m}Xe, ^{133}Xe, and ^{135}Xe) help in discriminating steady state reactor operations from nuclear tests. A new coincidence-based detection system using stilbene and strontium iodide [SrI_2(Eu)] for electron and photon detection respectively was developed at Oregon State University to address some of the challenges of the radioxenon systems deployed in the field such as memory effect, and poor energy resolution. Silicon photomultipliers (SiPMs) were used for detecting optical photons from all scintillation media. Real-time coincidence identification was achieved using the eight-channel digital pulse processor. The detection system was evaluated using lab check sources and Oregon State TRIGA reactor irradiated xenon samples. A 48-hour background coincidence spectrum was collected yielding a coincidence count rate and background rejection rate of 0.0174 ± 0.0003 counts per second (cps) and 98.9% respectively. The minimum detectable concentration (MDC) of the system was evaluated to be 0.11, 0.13, 0.20, and 0.73 mBq/m^3 for ^{131m}Xe, ^{133m}Xe, ^{133}Xe, and ^{135}Xe, respectively. The memory effect of the detection system was found to be 0.069 ± 0.015%, which is almost a 70-fold reduction compared to traditional plastic scintillators. The detection elements, custom-designed electronics, and the detector response to radioxenon are detailed in this work.

Keywords: Coincidence Detection; CTBT; Nuclear Explosion Monitoring; Radioxenon; SrI_2(Eu); Stilbene

PNNL release number: PNNL-SA-167137; LLNL Release number: LLNL-JRNL-827937

1. Introduction

The Comprehensive Nuclear-Test-Ban Treaty (CTBT) bans the testing of nuclear weapons anywhere on Earth [1, 2]. This includes underwater, underground, surface, and atmospheric testing. As of mid-2021, a total of 185 countries have signed this treaty out of which 170 countries have already ratified this treaty [3]. In an effort to develop an effective monitoring mechanism to ensure that countries are abiding by their treaty obligations, the Comprehensive Nuclear-Test-Ban Treaty Organization (CTBTO) operates the International Monitoring System (IMS). Eighty of the planned 321 monitoring stations will be equipped with radionuclide monitoring capabilities, out of which 40 will be additionally retrofitted with noble gas detection systems [4].

Identifying an underground explosion generally proves to be challenging since most of the traditional signatures from a nuclear explosion are concealed by the subsurface nature of the event. This is the primary reason the international community relies on other means to identify subsurface nuclear weapon explosions [5]. In an underground explosion, a large fraction of radionuclides generated in the fission process does not end up reaching the surface of the earth, making it difficult to readily identify a subsurface nuclear weapon explosion. Some xenon isotopes are of importance to the sub-surface explosion community because of their inert chemical nature, large fission yield, coincidence decay scheme, and ideal half-lives [6, 7]. It must be noted that although normal reactor operations also produce xenon isotopes, the ratio of xenon production from a weapon explosion and steady state reactor operations are significantly different, this enables possible indications of nuclear weapon explosions [8, 9]. It must however be pointed out that radioxenon releases from reactor start up, shutdown, and the operation of medical isotopes production facilities can mimic a nuclear explosion. Table 1 shows the prominent decay energies, branching ratios, and half-lives for the radioxenon of interest [10].

Table 1 Radiological properties of ^{131m}Xe, ^{133m}Xe, ^{133}Xe, and ^{135}Xe [10]

Isotope		Decay energy (keV)	Branching ratio (%)
^{131m}Xe ($t_{1/2}$ = 11.93 days)			
X-Rays	XKα_2	29.46	15.4
	XKα_1	29.78	28.6
	K'β_1	33.60	10.2
	K'β_2	34.61	1.85
Gamma rays		163.93	1.95
Conversion electrons		129.4	61
Coincident decays		X-ray and 129 keV e^-	56.1
^{133}Xe ($t_{1/2}$ = 5.35 days)			

X-Rays*	XKα_2	30.62	14.1
	XKα_1	30.97	26.2
	K'β_1	35.00	9.4
	K'β_2	36.01	1.7
Gamma rays		80.99	37
Conversion electrons		45	55.1
Betas (max energy)		346	100
Coincident decays		X-ray + 45 keV e^- + 346 keV beta	48.9
		81 keV gamma + 346 beta	37.2
^{133m}Xe ($t_{1/2}$ = 2.19 days)			
X-Rays	XKα_2	29.46	16.1
	XKα_1	29.78	29.8
	K'β_1	33.60	10.6
	K'β_2	34.61	1.9
Gamma rays		233.2	10
Conversion electrons		198.7	64
Coincident decays		X-ray and 199 keV e^-	58.4
^{135}Xe ($t_{1/2}$ = 0.38 days)			
X-Rays*	XKα_2	30.62	1.45
	XKα_1	30.97	2.69
	K'β_1	35.00	0.97
	K'β_2	36.01	0.185
Gamma rays		249.8	90
		608.2	2.9
Conversion electrons		214	5.7
Betas (max energy)		910	100
Coincident decays		X-ray + 214 keV e^- + 910 keV beta	5.7
		249.8 keV gamma + 910 keV beta	90

***The X-rays from the decay of ^{133}Xe and ^{135}Xe are originating from the Cs electron shell.**

During the late 1990s and early 2000s four countries (the United States of America, France, Sweden, and Russia) volunteered to develop radioxenon detection systems that collect the atmospheric air, separates xenon gas, purify the xenon sample, and quantify the activity of each xenon isotope of interest. These systems include the American Automated Radioxenon Sampler/ Analyzer (ARSA) developed by the Pacific Northwest National Laboratory (PNNL), the Swedish Automatic Unit for Noble gas Acquisition (SAUNA) designed by the Swedish Defense Research Agency (FOI), and the Russian Analyzer for Xenon Radioisotopes (ARIX) developed by the Khlopin Radium Institute that rely on electron-photon coincidence using NaI and plastic scintillators [11-17]. The initial French Système de Prélèvement Automatique en Ligne Avec l'Analyse du Xénon (SPALAX™) developed by the French Atomic Energy Commission (CEA)

functioned on high-resolution spectral analysis using HPGe detectors, however, later versions pivoted towards a coincidence-based design [18, 19]. It must be mentioned that some of these detection systems have been successful in identifying the nuclear tests carried out by the Democratic People's Republic of Korea and the releases from the Fukushima accident [20-27]. There have also been numerous attempts in the past by research groups around the world to develop either a coincidence or a single channel radioxenon detection system [28-35].

Although these systems feature high detection efficiencies (ARSA, SAUNA), and offer high spectral energy resolution for photons (SPALAX™), the state-of-the-art detection systems suffer from several drawbacks like the use of archaic technologies, memory effect, complex gain matching, and high maintenance cost. The scientific community has offered two solutions to reduce the memory effect, this includes either performing surface treatment to the inner walls of the gas cell or using new materials which are proven to be effective in reducing the memory effect [36-38].

Several radioxenon detection systems were developed at Oregon State University to improve on some of the drawbacks identified in the state-of-the-art detectors. The **T**wo **E**lement **C**d**Z**n**T**e (TECZT) detection system was developed using two 1 cm^3 face-to-face CZT crystals operating in coincidence. This detector offered excellent photon energy resolution but suffered from extensive electron backscatter [39, 40]. The **C**ZT crystal, an **A**rray of **S**iPMs, and a **P**lastic scintillator (CASP) detection system was developed using a CZT in conjunction with a plastic scintillator to detect photons and electrons in coincidence respectively. This design helped mitigate electron backscatter but introduced a memory effect in the detection system [41, 42]. To solve the challenge of the memory effect, a stilbene gas cell was used in place of a plastic scintillator [43-45]. This design reduced the memory effect compared to conventional plastic scintillators, but low coincidence efficiencies led to relatively poor minimum detectable concentrations (MDCs). Other electron detection media like PIPSBox were also explored in conjunction with CZT and SrI_2(Eu) [46-48]. Some of the key performance metrics of these detection systems are presented in Table 2. It is worth mentioning that unless specified, the ARSA detection system gas processing parameters were used for MDC calculations.

Table 2 Performance evaluation of some prototype radioxenon detection systems [39-48]

Parameters		**TECZE**	**CASP**	**Stilbene-CZT**	**PIPS-CZT**	**PIPS-SrI_2(Eu)**
Energy Resolution (%)	31 keV	48.2	30	25.8	35.8	24.0
	81 keV	12.5	12.8	9.3	12.6	12.9
	250 keV	4.4	5.7	4.2	5.3	8.1
	129 keV CE	10.1	23.7	20.2	13.4	9.6

Background Coincidence Count Rate (cps)		0.004	0.003	0.002	0.057	0.076
Memory Effect (%)		N/A	N/A	0.045	0.256	0.318
MDC (mBq/m^3)	^{131m}Xe	1.45	0.59	0.48	1.04*	0.12*
	^{133m}Xe	1.85	0.17	0.38	1.12*	0.15*
	^{133}Xe	0.51	0.84	0.84	0.61*	0.26*
	^{135}Xe	1.47	4.32	3.34	2.99*	1.00*

*Xenon International gas processing parameters were used for MDC calculations.

This research attempts to address some of the challenges observed in the state-of-the-art detectors by using modern materials and signal processing technologies. A stilbene gas cell is proposed in the capacity of an electron detector and SrI_2(Eu) is planned to be used for photon detection. Both stilbene and SrI_2(Eu) offer marginally improved energy resolution for conversion electrons and photons respectively compared to the state-of-the-art detection systems deployed on the IMS network. The primary goal of the research is to characterize the stilbene-SrI_2(Eu) detection system using the four radioxenons of interest, followed by evaluating the memory effect and calculating the MDC of the system. The individual detection elements, pulse processing electronics, and the experimental setup are detailed in this work.

2. Detector Design, Measurement Setup, and Individual Detector Characterizations

This prototype stilbene-SrI_2(Eu) detection system consists of three independent detection bodies: a well-type stilbene gas cell and two SrI_2(Eu) detection bodies. Photons from the stilbene gas cell are detected by a 2 × 2 SensL J-series SiPM array; two such arrays are used in each SrI_2(Eu) detector [49]. To identify coincidence events in real-time, an eight-channel Field Programmable Gate Array (FPGA) based digital pulse processor (DPP8) that was previously designed at Oregon State University was used for this work [50]. The signals from the stilbene SiPM array were routed through a preamplifier before being read by one of the channels in the DPP8. The signals from the SrI_2(Eu) SiPM arrays were routed through a charge sensitive preamplifier before being read by two independent channels in the DPP8. Coincidence events from either of the SrI_2(Eu) detectors and the stilbene gas cell are identified as valid events. It must also be pointed out that under some unique scenarios, all three detectors might trigger resulting from a photon backscatter. The coincidence identification mechanism was set such that these events are also recorded. Pulses identified in coincidence are then transferred to the PC to be analyzed by MATrix LABoratory (MATLAB) software for amplitude estimations and data plotting [51]. The entire detection system was held in place by a holder designed and printed at Oregon State University. Fig. 1a shows the SolidWorks cut-section view of the stilbene-SrI_2(Eu)

detection system. The assembled detection system inside the aluminum housing is shown in Fig. 1b.

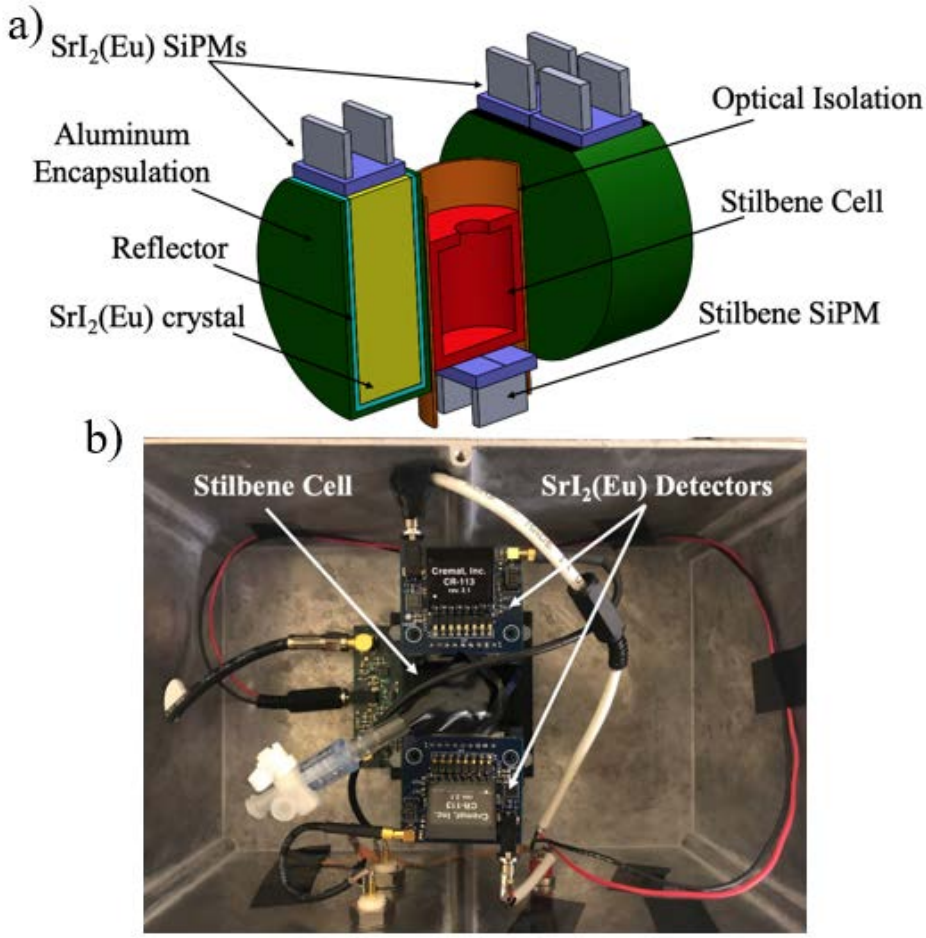

Fig. 1. a) SolidWorks cut section view of the radioxenon detection system; b) the assembled stilbene-$SrI_2(Eu)$ detector

2.1. Stilbene Gas Cell

The gas cell for this research that also acted in the capacity of an electron detector was fabricated using stilbene. Stilbene has several noticeable advantages over conventional plastic scintillators like improved energy resolution (20.2% vs 23.7% at 129 keV) and near-zero memory effect (0.04% vs 5%) [42, 43]. A custom stilbene gas cell was manufactured by Inrad Optics for this work. The body and two end caps were initially fabricated after which they were attached to form the complete gas cell [52]. A hole was machined on the top end cap to accommodate an outward-facing barb that attaches to the gas injection tube. A 3-way Luer lock was attached to

the other end of the tube to facilitate gas injection and vacuum generation. This Luer lock is also responsible for ensuring that the xenon gas does not leak after being injected into the gas cell for extended measurements. The gas cell has an external diameter of 18.7 mm and a wall thickness of about 1.8 mm. The total height of the gas cell was 21.7 mm with each end cap measuring about 2 mm. MCNP simulations were performed to ascertain that the 1.8 mm thick wall of the gas cell doesn't significantly attenuate the low energy X-rays. An attenuation of about 5.4% was observed. The gas cell has a volume of about 3.17 cm^3 and a solid angle of about 3.9 π. Polytetrafluoroethylene (PTFE) was wrapped around the external surface of the gas cell to improve the light collection. A single ARRAYJ-60035-4P-PCB SiPM was used for optical photon readout. Any additional surface area on the bottom stilbene end cap was painted with white reflective paint to further improve light collection.

2.2. SrI_2(Eu) Detectors

SrI_2(Eu) was chosen for this research in the capacity of a photon detector for several reasons including, high optical photon yield, relatively good energy resolution, low intrinsic background, and appreciable emission spectrum matching with the SensL J-series SiPMs. For photon detection, two custom SrI_2(Eu) detectors were fabricated by CapeSym Inc. [53]. Five percent Eu^{2+} doping was used by the manufacturer to further improve the optical photon yield of the scintillator. Each detector measured about 38.11 mm in diameter and 12.7 mm in thickness. A lateral cut was machined at about 14 mm from the center of each crystal to accommodate a pair of ARRAYJ-60035-4P-PCB SiPM arrays for optical photon readout. A PTFE reflector was used to cover all the sides of the scintillator except the face accommodating the SiPM arrays to improve the light collection. A 0.5 mm thick aluminum encapsulation was used to prevent moisture uptake by the crystal. Since SrI_2(Eu) is a hygroscopic material, it was required to use an airtight epoxy to prevent any moisture pickup by the crystal. This epoxy also prevents any external optical photons from interacting with the SiPMs, reducing the noise of the output signal. A 9-pin dual-in-line (DIL) female socket was used to connect the anode pins on the SiPMs to the custom-designed printed circuit board (PCB) featuring the charge-sensitive preamplifier for signal processing. The DIL sockets also perform the function of powering the cathodes on board the SiPM arrays.

2.3. SiPM Array

SiPMs in their most basic essence are reverse biased photodiodes operating in the Geiger mode. Each SiPM array consists of thousands of photodiodes (pixels) that can be individually fired by a single photon. When this device is coupled to a scintillator, the current signal generated is proportional to the number of optical photons impinging on the SiPM surface which is

proportional to the energy deposited by the ionizing radiation in the scintillation medium. SiPMs were chosen in this work as opposed to conventional PMT for several reasons including low operational voltage, modular design, improved ruggedness, low cost, and relative insensitivity to external electric and magnetic fields. For this work, a 2 × 2 array style SensL J-Series SiPM was mounted on the custom-designed PCB to read optical photons from the stilbene gas cell. As for the photon detector, SiPM arrays were directly mounted on the $SrI_2(Eu)$ crystal for optical photon readout. These SiPM features a microcell fill factor of about 75% and quantum efficiency of about 38% at 420 nm (2.5 V overvoltage). Fig. 2a shows the $SrI_2(Eu)$ detector along with the reflector, aluminum encapsulation, and the SiPM arrays. The $SrI_2(Eu)$ detectors used in the research are shown in Fig. 2b.

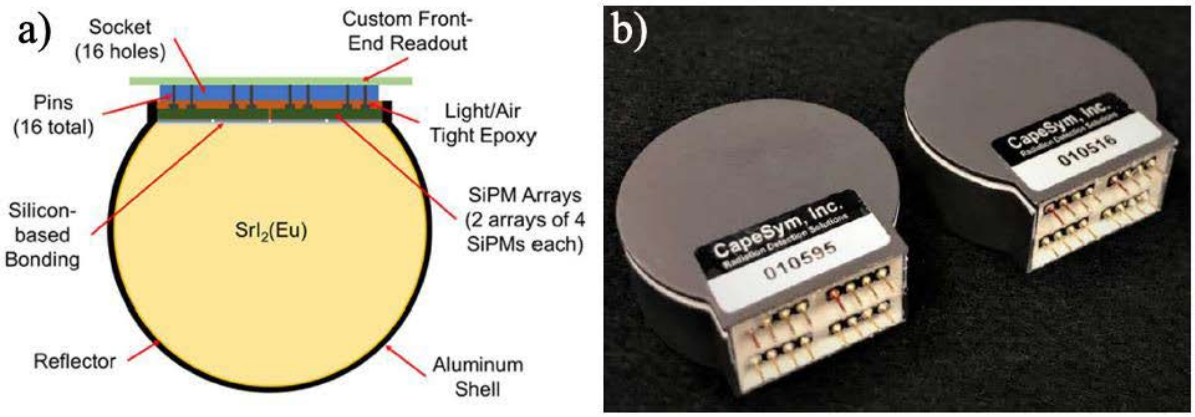

Fig. 2. a) cut section view of the $SrI_2(Eu)$ detector showing the SiPM array placement, optical photon reflector, and the Al encapsulation; b) the $SrI_2(Eu)$ detectors used in this work for photon detection

2.4. Readout Electronics and Pulse Processing

A custom PCB was designed at Oregon State University for signal readout from the stilbene SiPM array. Female sockets were machined on the board to enable direct mounting of the SiPM array. These sockets performed the task of both powering the SiPM array as well as reading the signals from the anode pins. A 3.3 V low dropout voltage (LDO) regulator was used to power the preamplifiers. For powering the SiPM cathodes, an LT8410 switching regulator was used to step up the +5V input signal to about +28.5 V [54]. The current signal from the stilbene SiPM array was then routed through the non-inverting preamplifier before being read by one of the channels in the DPP8. For the stilbene detector, the baseline is initially estimated followed by digitally integrating the pulse over 600 ADC values (4.8 μs). This integrated value is subsequently mapped to a channel in the spectrum.

In-house designed PCBs were used for reading signals from the $SrI_2(Eu)$ detectors. A switching regulator (LT8410) was used to initially step up the voltage from +5V to about +27.5V, this voltage signal was routed to all the cathode pins to power the SiPM array. The anode pin signals were routed through a Cremat Inc. CR-113 charge sensitive preamplifier (CSP) with a time constant of 50 μs [55]. Since $SrI_2(Eu)$ has a decay time between 1 and 5 μs, using a CSP with about a 10-fold increase in the decay time of the scintillator is sufficient to integrate the entire pulse. The pulse output is then routed through a series of MMCX and BNC connectors before being read by two channels of the DPP8 (one channel per detector). To determine the energy deposited by the radiation photon in the scintillator, a trapezoidal filter was realized in MATLAB, and a flat-top and peaking time of 9.6 and 4.8 μs respectively was used in the work.

The DPP8 houses a custom-designed 8 channel readout board to convert the analog signals to the digital domain, this is accomplished by using a 14-bit, 125 MHz ADC onboard the processor. The digitized signals are then routed through the commercially off-the-shelf Opal Kelly board [56]. The near real-time coincidence identification is implemented using the Xilinx Kintex-7 FPGA [57]. For this research, a coincidence time window of about 4.4 μs was used based on previous research experience. Once the coincidence events are identified, the pulse data of each channel of interest is transferred to the MATLAB user interface. Amplitude identification of individual pulses followed by spectral plotting is carried out in the MATLAB user interface.

3. Experimental Work

3.1. Detector Calibration and Sample Preparation

Based on prior experience with working on stilbene/plastic gas cells it was observed that even after securely coupling the gas cell and the SiPM arrays, external optical photon interactions often cause the SiPM pixels to fire, resulting in a noisy baseline. To remedy this, multiple layers of black masking tape were wrapped around the outward-facing barb of the stilbene gas cell. In addition to this, a thin cylindrical ring was designed, and 3D printed to optically isolate the stilbene cell + SiPM array.

A 10 μCi ^{137}Cs disk source was used to calibrate the photon detectors. It was found that one of the $SrI_2(Eu)$ detectors was about 1.8 times brighter than the other. The brighter scintillator yielded a resolution of 19.8% and 7.6% for the 31 keV X-ray and the 662 keV gamma photon respectively. An energy resolution of 27.3% and 6.6% was determined for the 31 and 662 keV photons respectively using the dimmer scintillator. A variable energy X-ray source was used to determine the threshold of the photon detectors. Based on the results, an energy threshold of about 20 keV was set for both $SrI_2(Eu)$ detectors. To establish that the detectors were

appropriately gain matched, an experiment was conducted to record a coincidence spectrum between the $SrI_2(Eu)$ detectors using a ^{137}Cs check source placed in-between the two bodies at equidistance. Fig. 3 shows the 2D coincidence spectrum that was obtained using this experimental setup. Most of the counts in the coincidence spectra were concentrated at two locations corresponding to about 480 and 190 keV along either axis. It is worth mentioning that the Compton edge of the 662 keV gamma photon is observed at about 477 keV and the backscattered photon carries the remaining energy of about 185 keV. Connecting a straight line between these two hotspots results in the x and y-axis intercepts at about 660 keV. This demonstrates that the photon detectors are both calibrated and gain matched.

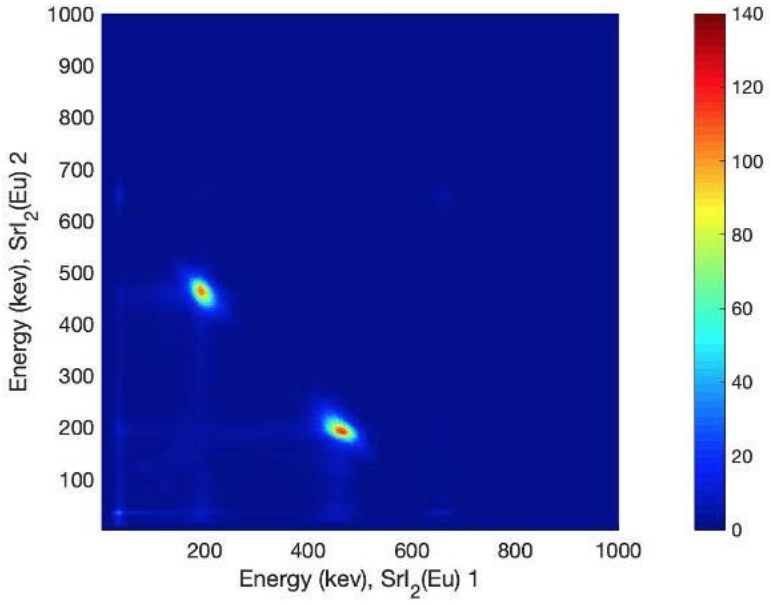

Fig. 3. 2D backscatter coincidence spectrum from the $SrI_2(Eu)$ detectors using a ^{137}Cs disc source

After this, both the electron and photon detectors were calibrated in coincidence. This was performed using the Compton backscatter line from the electron and photon detectors using the 662 keV photon from a ^{137}Cs source. Fig. 4 shows the 2D coincidence spectrum recorded using this setup. A straight diagonal feature with intercepts at about 660 keV along both the axis establishes that the detection system was well calibrated. Some events with energy deposition of about 450 keV and 150 keV were recorded in the photon detector. These events were attributed to the Compton edge or backscatter photon interactions in the $SrI_2(Eu)$ detection medium or surrounding material (shielding/ detector housing) in coincidence with minimal energy deposition in the electron detector. The energy thresholds for the electron and photon detectors were set at 30 and 20 keV respectively.

Radioxenon samples were prepared by loading 1-3 ml of commercially available pure mono-isotopic xenon in polystyrene syringes. A 3-way Luer lock was used at the end of the syringe to ensure minimal xenon leakage. This was followed by irradiating these samples in the Oregon State University TRIGA reactor thermal column. The samples were exposed to a thermal neutron flux of about 7 x 10^{10} n cm^{-2} sec^{-1} for 7 hours. The samples were then cooled for about 16 hours before being injected into the stilbene cell to reduce pileup. Three irradiation runs were performed in total for each radioxenon of interest.

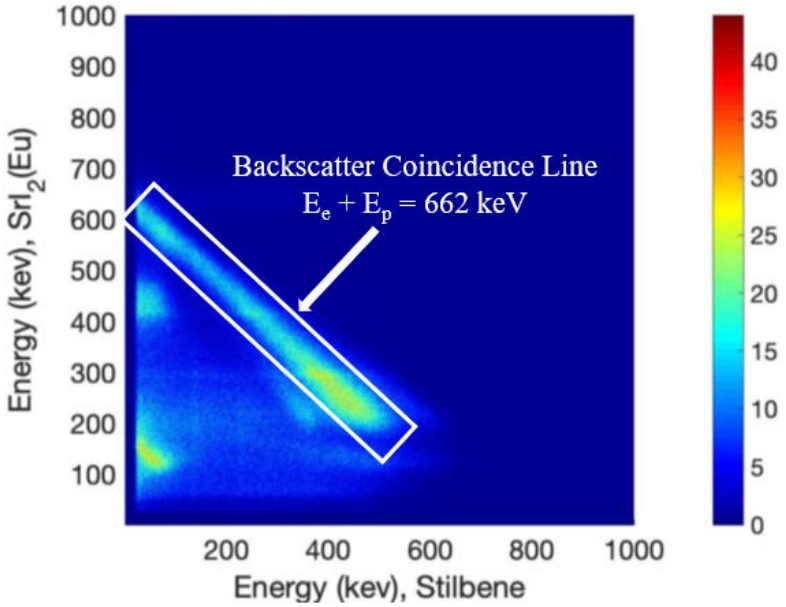

Fig. 4. The coincidence backscatter spectrum from stilbene and SrI_2(Eu) using a ^{137}Cs source

3.2. Absolute Coincidence Detection Efficiency Calculations

Coincidence detection efficiencies play a vital role in the MDC calculations. These values can either be obtained using simulation or experimental methods. In this work, an attempt was made to experimentally determine some of these values [58]. Since the exact activity of the sample couldn't be determined during injection, the equations described in Cooper et al. were utilized [59]. This method employs the electron/photon singles and coincidence count rate to calculate the efficiencies. The absolute efficiency equations are presented in equations 1-3.

$$A_T = \frac{C_{\beta\gamma}}{\epsilon_{\beta\gamma} BR_{\beta\gamma}} = \frac{C_{\beta\gamma}}{\epsilon_{\beta\gamma} BR_{\gamma}} = \frac{C_{\beta\gamma}}{BR_{\gamma} \epsilon_{\beta} \epsilon_{\gamma}} \quad (1)$$

$$A_T = \frac{C_{\gamma}}{\epsilon_{\gamma} BR_{\gamma}} \quad (2)$$

$$A_T = \frac{C_\beta}{1-(1-\epsilon_\beta)(1-\epsilon_{CE_i} BR_{CE_i})} \quad (3)$$

Where, C is the total count rate from the electron detector, photon detector, or both these detectors in coincidence. BR is the branching ratio of the decay of interest. ϵ is the detection efficiency of the electron detector, photon detector, or both these detection media in coincidence. All the beta emissions occur with a 100% branching ratio accompanied by a photon in coincidence, this allows us to set the beta branching ratio to unity. Calculating the photon efficiency requires the consideration of variable decay paths and their efficiencies.

3.3. *Energy Calibration and Detector Response using ^{131m}Xe*

Xe131m emits a 30 keV X-ray, 164 keV gamma photon, 129, and 159 keV conversion electrons. Out of these emissions, the 30 keV X-ray and the 129 keV conversion electron are observed in coincidence. This xenon isotope is unique among the isotopes of interest because of its mono energetic coincidence emissions for both the electrons and photons. This provides a unique opportunity for researchers to accurately calibrate the electron detector. The summed stilbene and SrI_2(Eu) spectra in coincidence mode are shown in Fig. 5a and Fig. 5b respectively. An energy resolution of 35.7% and 23.6% FWHM were obtained for the electron and photon detectors respectively. The 2D coincidence spectrum for ^{131m}Xe is shown in Fig. 5c, since both the electron and photon emissions are monoenergetic in nature, a confined region was observed in the 2D spectrum.

For absolute efficiency calculations, the number of counts under each peak are required to be estimated for the conversion electrons (129 and 159 keV) in singles mode. Since the stilbene detector was unable to resolve the counts under each individual peak, it was decided to use MCNP6 simulated efficiencies for the 129 and 159 keV conversion electrons. Using the electron singles count rate and the conversion electron branching ratios, the total activity was calculated. An X-ray efficiency was determined by equating the total activity to the X-ray singles count rate and the respective branching ratio. Table 3 shows the absolute efficiency calculated for ^{131m}Xe.

Table 3 Absolute coincidence detection efficiency determined using ^{131m}Xe

Region of Interest	Absolute Efficiency (%)
31 keV X-ray + 129 keV Conversion Electron	10.0 ± 0.4

3.4. *Detector Response using $^{133/133m}Xe$*

The irradiation of ^{132}Xe produces two xenon isotopes: ^{133m}Xe, and ^{133}Xe. Xe133m releases a 199 keV conversion electron in coincidence with a 30 keV X-ray. Xe133 has two decay schemes, a

45 keV conversion electron in coincidence with a 30 keV X-ray and 0-346 keV β, and an 81 keV gamma photon in coincidence with a 0-346 keV β. On the photon detection front, the 30 keV X-ray and the 81 keV gamma photon are uniquely identified. The summed coincidence energy resolution of 23.9% and 14.9% FWHM was determined for the 30 keV X-ray and the 81 keV gamma photon respectively. The 45 keV conversion electron was observed in coincidence with the 0-346 keV β particle and the 30 keV X-ray. The 81 keV gamma photon was uniquely identified in coincidence with the 0-346 keV β emission. The 1D coincidence spectra from the electron and photon detector are shown in Fig. 6a and Fig. 6b respectively. The 45 and 199 keV conversion electron features can be slightly observed in the electron spectrum (Fig. 6a). The 2D coincidence spectrum (Fig. 6c) shows two unique regions of interest at the X-ray and gamma photon energies. To better observe the spectral features of the 45 and 199 keV conversion electrons, X-ray, and gamma gated electron spectra are presented in Fig. 7a and Fig. 7b respectively. The conversion electron peaks superimposed on the beta continuum (Fig. 7a), and the pure beta continuum (Fig. 7b) are clearly observed in these spectra.

Absolute efficiencies were calculated for $^{133m/133}$Xe by using the methods described previously. Since the number of counts under the 199 keV and 45 keV conversion electron peak could not be determined, it was decided to use simulated efficiencies using MCNP6. A threshold of 30 keV was employed as part of these calculations. The efficiency for the 0-346 keV β was determined by computing the ratio of the coincidence and singles count rate from SrI_2(Eu) in the region of interest. The electron singles count rate, the efficiency of the conversion electron and the beta particle were used to determine the total activity in the sample. This value was equated to the gamma branching ratio and the singles count rate to determine the 81 keV gamma photon efficiency. Table 4 shows the efficiencies for the $^{133m/133}$Xe regions of interest.

Table 4 Absolute coincidence detection efficiencies for the regions of interest from $^{133m/133}$Xe

Region of Interest	Absolute Efficiency (%)
31 keV X-ray + 199 keV Conversion Electron	10.8 ± 0.3
81 keV gamma + 0-346 keV β	17.8 ± 0.1
31 keV X-ray + (45 keV Conversion Electron × 0-346 keV β)	8.4 ± 0.2

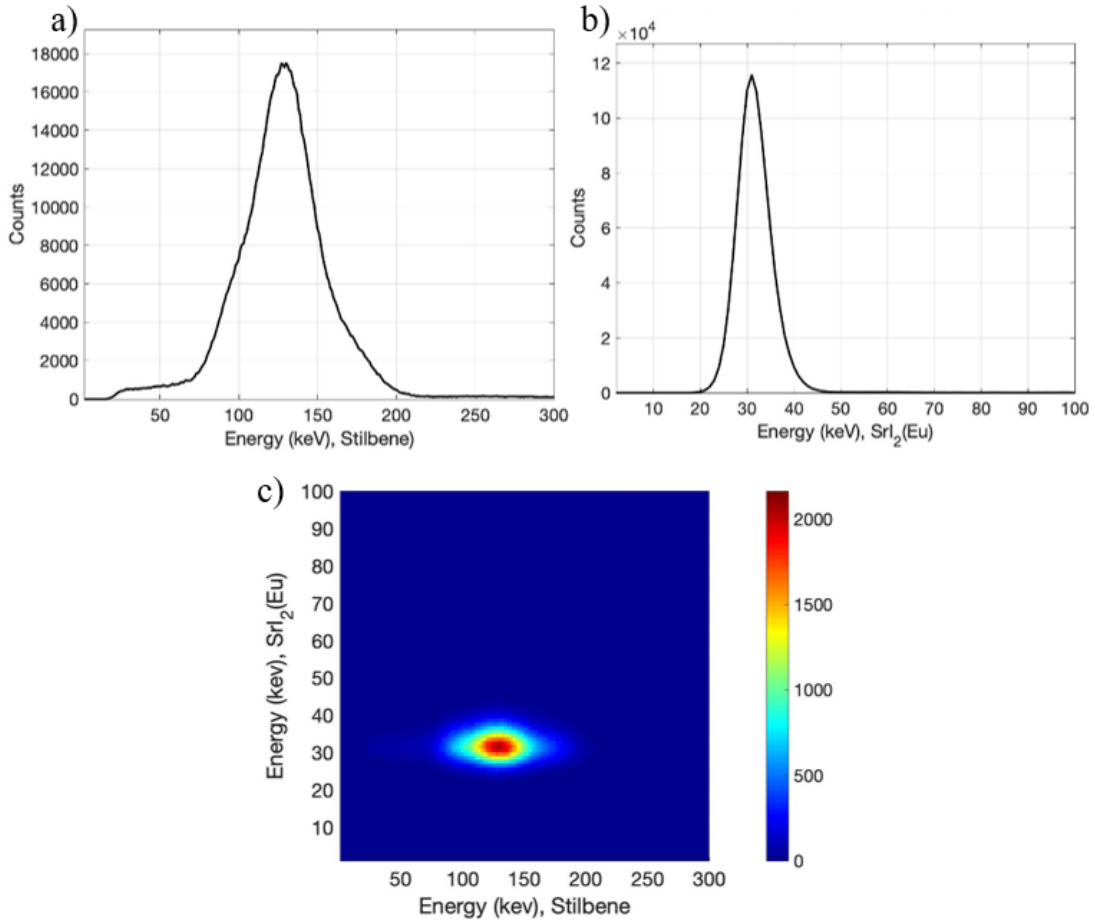

Fig. 5. Coincidence results from ^{131m}Xe; (a) 1D spectrum from the stilbene detection medium showing the 129 keV conversion electron; (b) summed SrI_2(Eu) detector response to the 30 keV X-ray; (c) 2D spectrum illustrating a confined region of interest

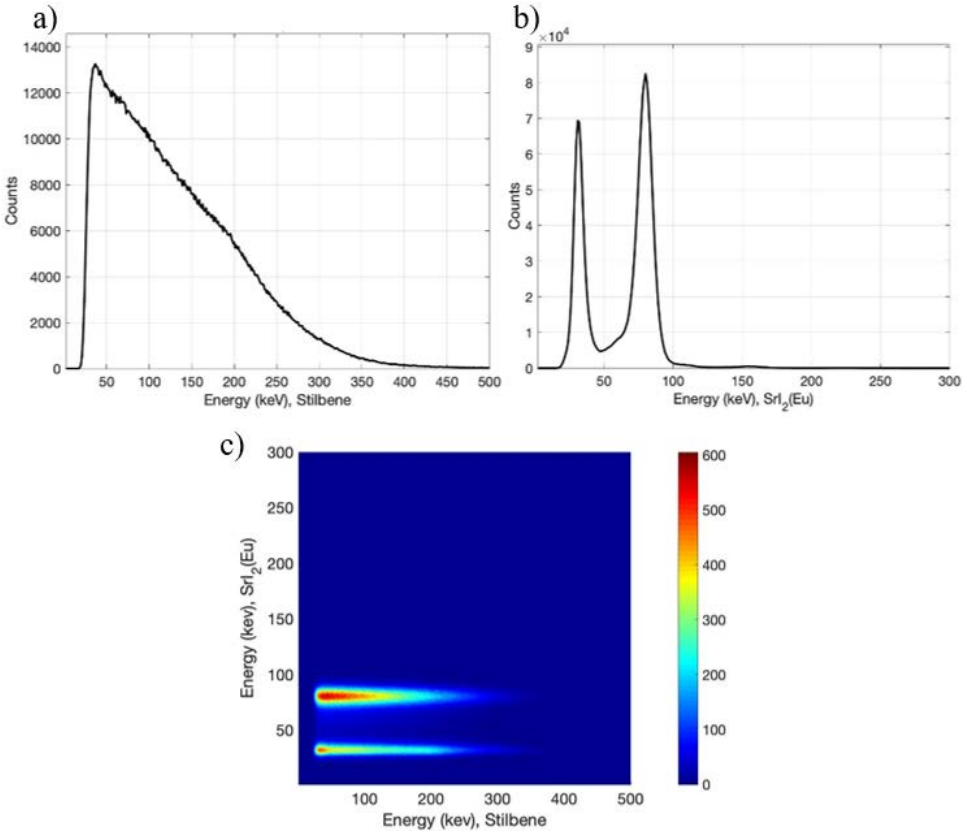

Fig. 6. Coincidence results from $^{133m/133}$Xe; (a) 1D spectrum from the stilbene detection medium illustrating the 45 and 199 keV conversion electrons on top of a 0-346 keV β continuum; (b) summed 1D SrI_2(Eu) detector response from the 30 and 81 keV photons; (c) 2D spectrum showing two clear regions of interest corresponding to the X-ray and gamma photon

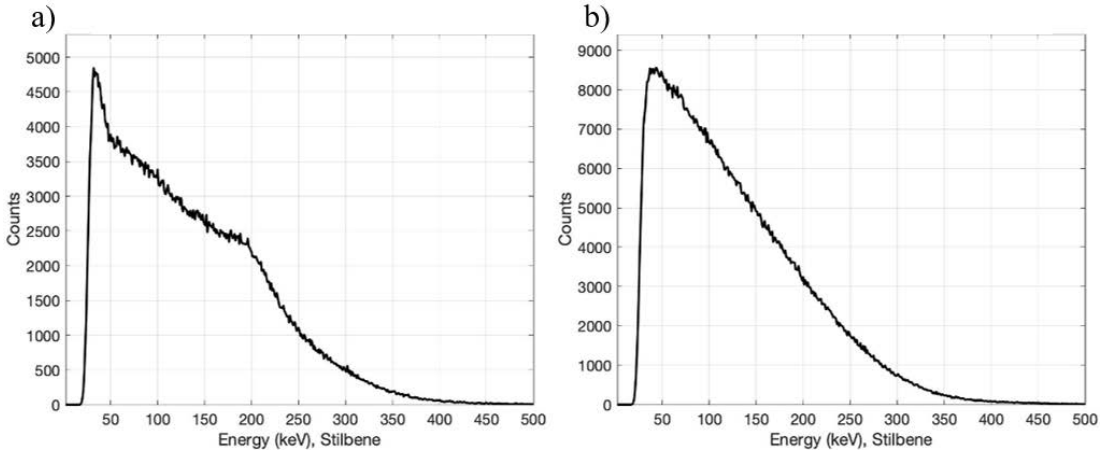

Fig. 7. Photon gated $^{133m/133}$Xe coincidence spectra showing; a) the 45 and 199 keV conversion electrons (X-ray gated); b) 0-346 keV β continuum (gamma gated)

3.5. Detector Response using ^{135}Xe

Xe135 emits a 0-910 keV β in coincidence with a 250 keV gamma photon. This xenon radionuclide of interest has the shortest half-life of about 9.2 hours. These features were uniquely observed in the 1D electron and photon coincidence spectrum in Fig. 8a and Fig. 8b respectively. The energy resolution of the 250 keV gamma photon was determined to be 9.7% FWHM. Fig. 8c shows the 2D coincidence spectrum where most of the counts are concentrated in a narrow region around 250 keV on the y-axis representative of the gamma energy and stretching between 0 and 910 keV on the x-axis representative of the electron energy.

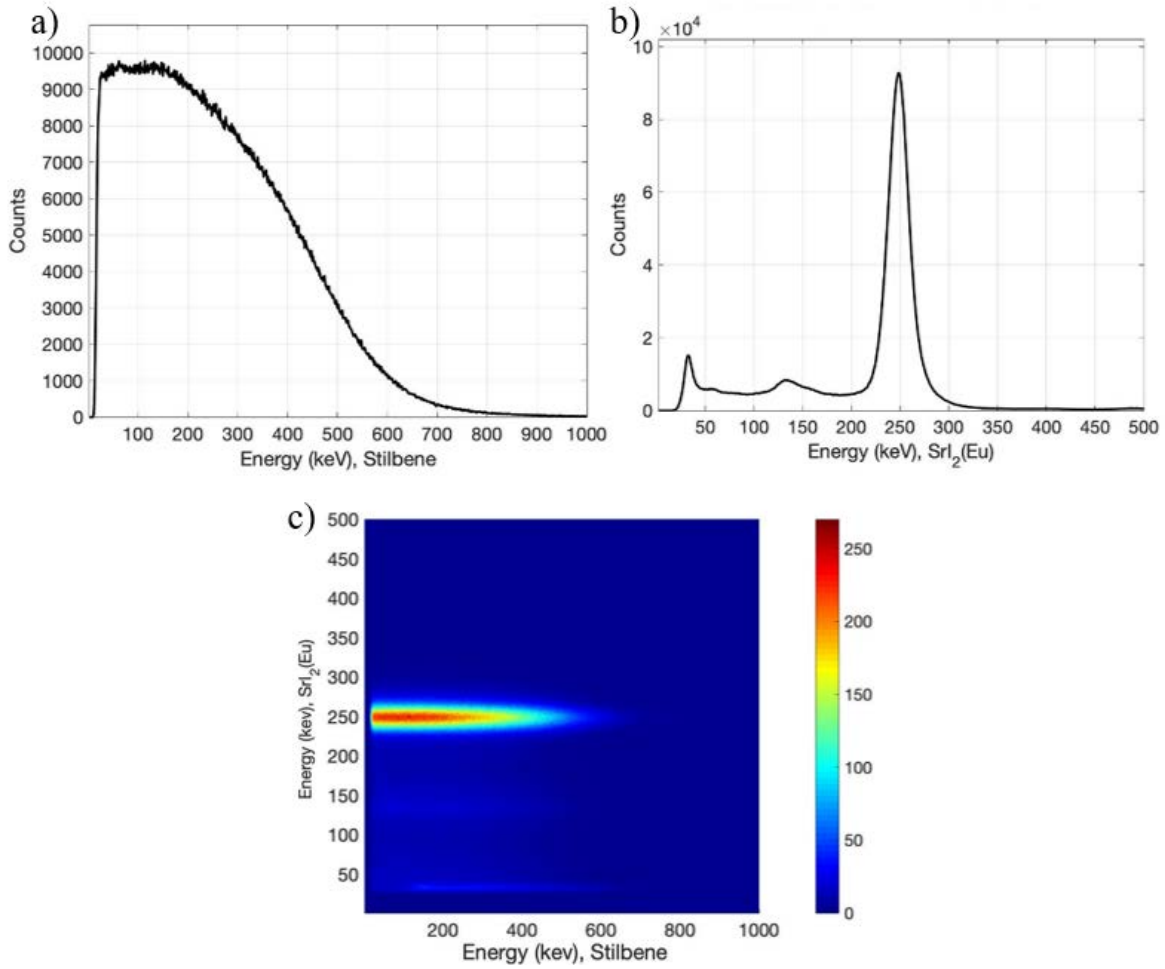

Fig. 8. Coincidence results from ^{135}Xe; (a) 1D spectrum from the stilbene detector showing the 0 to 910 keV β continuum; (b) summed detector response of the 250 keV gamma photon from $SrI_2(Eu)$; (c) 2D spectrum illustrating a confined region of interest

Absolute efficiency was calculated for the 250 keV gamma photon and the 0-910 keV β particle. Since in the calculation of MDC for ^{135}Xe, there is no dedicated region of interest for the X-ray and the 214 keV conversion electron because of its low branching ratio, these efficiencies were not calculated. The 0-910 keV β particle efficiency was determined by the ratio of the coincidence and singles count rate from SrI_2(Eu). The total sample activity was compared to the branching ratio and the gamma singles count rate to determine the gamma photon efficiency. The coincidence detection efficiencies for ^{135}Xe are presented in Table 5.

Table 5 Absolute coincidence detection efficiency for ^{135}Xe

Region of Interest	Absolute Efficiency (%)
250 keV gamma + 0-910 keV β	14.1 ± 0.2

3.6. Memory Effect

To observe the signatures from radioxenon, the gas sample is first injected into a plastic cell which generally also acts in the capacity of an electron detector. During the time the radioxenon signatures are captured, some of the xenon ends up diffusing through the walls of the plastic scintillator. Once the measurements are complete, the xenon gas in the cell is subjected to a vacuum to extract the sample. However, a small fraction of the gas sample remains in the walls of the gas cell leading to an elevated background in subsequent measurements, this phenomenon is called the memory effect. Literature has indicated that the crystalline structure of stilbene might be successful in eliminating this challenge. To evaluate the memory effect, ^{131m}Xe was chosen because of its relatively long half-life of about 11.93 days which would eliminate the need for decay corrections since the experimental procedure lasted for about an hour. These measurements were performed after allowing the ^{131m}Xe sample to reside in the gas cell for over a week. A tubing system was set in place to connect the gas cell to a roughing pump with a pressure gauge to monitor the pressure drop. Any challenges with regards to backflow were addressed by shutting the valve between the gas cell and the pump before powering down the roughing pump.

Memory effect evaluations were conducted right after collecting data from ^{131m}Xe. To estimate the memory effect, a baseline is initially required to be established. A fixed number of coincidence counts were collected, and the time to collect the counts was recorded, this helps in establishing the baseline count rate of the detection system. A 3σ full-width ROI was established around the peaks to estimate the counts during the baseline run [43]. This is followed by subjecting the gas cell to a vacuum using the roughing pump for about 5 minutes after which a fixed number of counts are recorded to estimate the count rate. The gas cell is then flushed with

air before subjecting it again to a vacuum for 5 minutes. Each run resulted in achieving a vacuum of about 5 torr. After seven such routines, a memory effect of about 0.069 ± 0.015% was observed. This is higher than the 0.045 ± 0.017% value obtained using the stilbene-CZT experimental setup but is within the prescribed error. The memory effect obtained using the stilbene-SrI_2(Eu) system is about seventy times lower than a typical plastic scintillator [60].

3.7. Background

A 48-hour background measurement was collected in coincidence mode with no radioxenon gas sample in the stilbene cell. About 3,007 coincidence counts were recorded in an energy range between 0 to 1,000 keV for the stilbene cell and 0 to 500 keV for the SrI_2(Eu) detector. A background coincidence rate and a background rejection rate of about 0.0174 ± 0.003 counts per second and 98.9% respectively were determined for the stilbene-SrI_2(Eu) detection system. The 48-hour background coincidence spectrum is shown in Fig. 9.

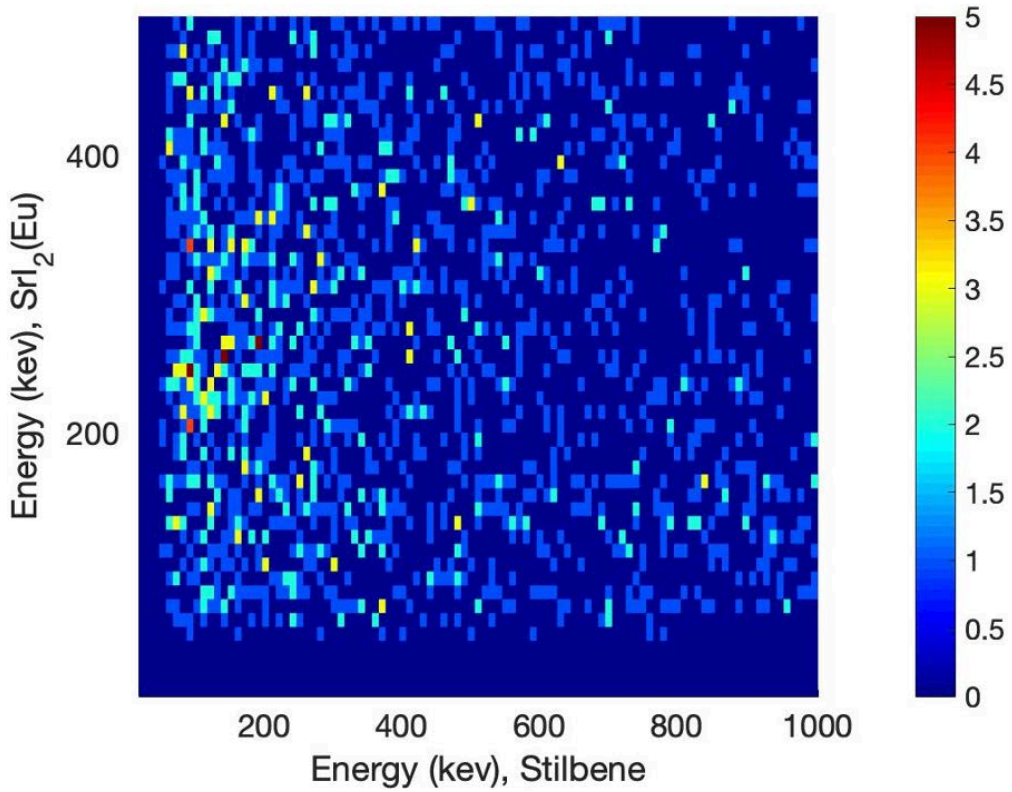

Fig. 9. A 48-hour background coincidence measurement using the stilbene-SrI_2(Eu) system

3.8. Minimum Detectable Concentration (MDC)

The MDC of a radioxenon detection system is the minimum amount of radioxenon that can be detected by the system with 95% confidence. For a system to be qualified to be deployed on the

IMS network, the detector needs to attain an MDC of under 1 mBq/ m^3 for ^{133}Xe. The MDC of a system is calculated according to equation 4 [61]:

$$MDC\left(\frac{mBq}{m^3 air}\right) = \left[\frac{2.71+4.65\sigma_0}{\varepsilon_\beta \varepsilon_\gamma \beta_{BR} \gamma_{BR}}\right]\left[\frac{\lambda^2}{(1-\exp(-\lambda T_c))(-\lambda T_p)(1-\exp(-\lambda T_A))}\right]\left[\frac{T_C * 1000}{V_{air}}\right] \quad (4)$$

Where:

$$\sigma_0 = \sqrt{\frac{TA}{Tb} BckCnt_{total} + \sigma^2_{BckCnt} + InterferenceCnt + \sigma^2_{InterferenceCnt} + MemoryCnt + \sigma^2_{MemoryCnt}} \quad (5)$$

- ε_β : Efficiency for detection of β
- ε_γ : Efficiency for detection of γ
- β_{BR} : Branching ratio of β
- γ_{BR} : Branching ratio of γ
- λ : Decay constant of isotope of interest [s^{-1}]
- T_c : Collection time of xenon sample [21,600 s]
- T_p : Processing time of gas [19,620 s]
- T_A: Counts acquisition time [86,400 s]
- V_{air} : Collected air volume [36 m^3]

And

- $BckCnt_{total}$*:* Summation of the total number of background counts observed in the ROI of interest
- InterferenceCnt: Counts due to interferences from radon daughters and overlapping ~30 keV regions of interest
- MemoryCnt: Counts due to memory effect
- *Tb*: Background measurement time [172,800 s]

The σ_0 term in the MDC equation consists of three components (equation 5). For this work, the memory effect was assumed to be zero since the background measurements were conducted after it was established that there was minimal residual activity in the gas cell and since a stilbene cell was employed, there was near-zero memory effect observed compared to a plastic gas cell. The radon interference counts were also assumed to be zero since pure xenon samples were irradiated in the Oregon State TRIGA reactor and injected in the gas cell rather than using atmospheric samples. It must also be noted that this MDC calculation is performed for a blank sample assuming any other interference to be zero. Therefore, after accounting for these factors, the σ_0 term in the MDC equation simplifies to:

$$\sigma_0 = \sqrt{\frac{TA}{Tb} BckCnt_{total} + \sigma^2_{BckCnt}} \quad (6)$$

A Poisson distribution was assumed for the background count error. This leads to the σ_{BckCnt} term being equal to the square root of the background counts in each ROI. The detection efficiencies for each region of interest are presented in Table 3, Table 4, and Table 5. Variables like the branching ratios for each radioxenon of interest are provided in Table 1. Values like T_C, T_P, T_A, and V_{air} are dependent on the gas processing parameters of the system. For this work, the gas processing parameters of the Xenon International system were utilized for MDC calculations [62, 63]. In terms of MDC calculations, since ^{133}Xe has two distinct decay paths, a weighted average of both the decay paths is required to be considered (equation 7).

$$MDC_{^{133}Xe}\left(\frac{mBq}{m^3\ air}\right) = \sqrt{\frac{1}{\left(MDC^{81\ keV}_{^{133}Xe}\right)^{-2} + \left(MDC^{30\ keV}_{^{133}Xe}\right)^{-2}}} \quad (7)$$

For the MDC calculations, a 3σ full-width ROI was defined around each monoenergetic peak, a 0 to β_{max} ROI was defined for the beta energies of interest. Since the 199 keV conversion electron's energy resolution could not be determined, it was decided to scale the resolution according to the results from the stilbene-CZT system and the 129 keV conversion electron resolution from the stilbene-SrI_2(Eu) system. Based on the background measurement that was collected, these regions of interest were applied to account for the total number of counts in each ROI. Table 6 shows the MDC calculated for the stilbene-SrI_2(Eu) detection system along with some other state-of-the-art radioxenon detectors.

Table 6 Comparison of MDC for various radioxenon detection systems

Radioxenon Isotope	Xenon International (mBq/m^3) [64]	SAUNA III (mBq/m^3) [65]	SPALAX-NG (mBq/m^3) [19]	Stilbene-SrI_2(Eu)* (mBq/m^3)
^{131m}Xe	0.15	0.25	0.1	0.11
^{133m}Xe	0.15	0.15	0.1	0.13
^{133}Xe	0.15	0.22	0.1	0.20
^{135}Xe	0.5	0.30	0.4	0.73

*A pure xenon sample (ideal sample) was used with no radon background

4. Conclusion

In this work, an evaluation of the stilbene - $SrI_2(Eu)$ radioxenon detection system was performed. Custom electronic readout was designed for both the electron and photon detectors. SiPMs were utilized for reading optical photons from the $SrI_2(Eu)$ detectors and the stilbene gas cell. Coincidence identification was performed in near real-time using a FPGA while the detection system was controlled using a MATLAB user interface. Initial calibration and characterization of the system was carried out using a ^{137}Cs lab check source. Ultra-pure xenon samples were irradiated in the Oregon State TRIGA reactor to produce radioxenon of interest. All the xenon isotopes of interest (^{131m}Xe, $^{133m/133}Xe$, and ^{135}Xe) were uniquely identified. A memory effect of about 0.069 ± 0.015% was determined for this system (about a 70-time reduction compared to conventional plastic gas cells). The MDC values of all four radioxenon were found to be below 1 mBq/m^3, thereby meeting the sensitivity requirements prescribed by the CTBTO. With an increase in the photon detector solid angle, further improvements in the detection efficiency and the MDC are anticipated.

5. Acknowledgments

Pacific Northwest National Laboratory is operated by Battelle Memorial Institute for the U.S. Department of Energy under Contract DE-AC05-76RL01830. This work was funded in part by the Consortium of Verification Technology (CVT) under Department of Energy National Nuclear Security Administration award number DE-NA0002534. Lawrence Livermore National Laboratory is operated by Lawrence Livermore National Security, LLC, for the U.S. Department of Energy, National Nuclear Security Administration under Contract DE-AC52-07NA2734

6. References

[1] Comprehensive Nuclear-Test-Ban Treaty Organization, Who We Are. https://www.ctbto.org/specials/who-we-are/ [Accessed: 7 Sep 2021]

[2] P.R.J. Saey, L.-E. De Geer, Notes on radioxenon measurements for CTBT verification purposes, Applied Radiation and Isotopes. 63 (2005) 765–773. https://doi.org/10.1016/j.apradiso.2005.05.035.

[3] Comprehensive Nuclear-Test-Ban Treaty Organization, Status of Signature and Ratification. https://www.ctbto.org/the-treaty/status-of-signature-and-ratification/ [Accessed: 7 Sep 2021]

[4] Comprehensive Nuclear-Test-Ban Treaty Organization, Press release. https://www.ctbto.org/press-centre/highlights/2017/2017-four-more-ims-stations-certified-in-china/ [Accessed: 7 Sep 2021]

[5] C.R. Carrigan, Y. Sun, Detection of Noble Gas Radionuclides from an Underground Nuclear Explosion During a CTBT On-Site Inspection, Pure and Applied Geophysics. 171 (2014) 717–734. https://doi.org/10.1007/s00024-012-0563-8.

[6] T.W. Bowyer, C. Schlosser, K.H. Abel, M. Auer, J.C. Hayes, T.R. Heimbigner, J.I. McIntyre, M.E. Panisko, P.L. Reeder, H. Satorius, J. Schulze, W. Weiss, Detection and analysis of xenon isotopes for the comprehensive nuclear-test-ban treaty international monitoring system, Journal of Environmental Radioactivity. 59 (2002) 139–151. https://doi.org/10.1016/S0265-931X(01)00042-X.

[7] C.R. Carrigan, R.A. Heinle, G.B. Hudson, J.J. Nitao, J.J. Zucca, Trace gas emissions on geological faults as indicators of underground nuclear testing, Nature. 382 (1996) 528–531. https://doi.org/10.1038/382528a0.

[8] M.B. Kalinowski, M.P. Tuma, Global radioxenon emission inventory based on nuclear power reactor reports, Journal of Environmental Radioactivity. 100 (2009) 58–70. https://doi.org/10.1016/j.jenvrad.2008.10.015.

[9] G. Le Petit, P. Armand, G. Brachet, T. Taffary, J.P. Fontaine, P. Achim, X. Blanchard, J.C. Piwowarczyk, F. Pointurier, Contribution to the development of atmospheric radioxenon monitoring, Journal of Radioanalytical and Nuclear Chemistry. 276 (2008) 391–398. https://doi.org/10.1007/s10967-008-0517-x.

[10] Brookhaven National Laboratory, National Nuclear Data Center. https://www.nndc.bnl.gov/ensdf/ [Accessed: 29 Sep 2021]

[11] J.I. McIntyre, K.H. Abel, T.W. Bowyer, J.C. Hayes, T.R. Heimbigner, M.E. Panisko, P.L. Reeder, R.C. Thompson, Measurements of ambient radioxenon levels using the automated radioxenon sampler/analyzer (ARSA), Journal of Radioanalytical and Nuclear Chemistry. 248 (2001) 629–635. https://doi.org/10.1023/A:1010672107749.

[12] M.W. Cooper, J.I. McIntyre, T.W. Bowyer, A.J. Carman, J.C. Hayes, T.R. Heimbigner, C.W. Hubbard, L. Lidey, K.E. Litke, S.J. Morris, M.D. Ripplinger, R. Suarez, R. Thompson, Redesigned β–γ radioxenon detector, Nuclear Instruments and Methods in Physics Research Section A: Accelerators, Spectrometers, Detectors and Associated Equipment. 579 (2007) 426–430. https://doi.org/10.1016/j.nima.2007.04.092.

[13] T.W. Bowyer, K.H. Abel, C.W. Hubbard, A.D. McKinnon, M.E. Panisko, R.W. Perkins, P.L. Reeder, R.C. Thompson, R.A. Warner, Automated separation and measurement of radioxenon for the Comprehensive Test Ban Treaty, Journal of Radioanalytical and Nuclear Chemistry. 235 (1998) 77–82. https://doi.org/10.1007/BF02385941.

[14] A. Ringbom, T. Larson, A. Axelsson, K. Elmgren, C. Johansson, SAUNA—a system for automatic sampling, processing, and analysis of radioactive xenon, Nuclear Instruments and Methods in Physics Research Section A: Accelerators, Spectrometers, Detectors and Associated Equipment. 508 (2003) 542–553. https://doi.org/10.1016/S0168-9002(03)01657-7.

[15] V.V. Prelovskii, N.M. Kazarinov, A.Yu. Donets, V.Yu. Popov, I.Yu. Popov, N.V. Skirda, The ARIX-03F mobile semiautomatic facility for measuring low concentrations of radioactive xenon isotopes in air and subsoil gas, Instruments and Experimental Techniques. 50 (2007) 393–397. https://doi.org/10.1134/S0020441207030165.

[16] Yu.S. Popov, N.M. Kazarinov, V.Yu. Popov, Yu.M. Rykov, N.V. Skirda, Measuring Low Activities of Fission-Product Xenon Isotopes Using the β-γ Coincidence Method, Instruments and Experimental Techniques. 48 (2005) 380–386. https://doi.org/10.1007/s10786-005-0066-2.

[17] M. Auer, T. Kumberg, H. Sartorius, B. Wernsperger, C. Schlosser, Ten Years of Development of Equipment for Measurement of Atmospheric Radioactive Xenon for the Verification of the CTBT, Pure and Applied Geophysics. 167 (2010) 471–486. https://doi.org/10.1007/s00024-009-0027-y.

[18] G. Le Petit, P. Armand, G. Brachet, T. Taffary, J.P. Fontaine, P. Achim, X. Blanchard, J.C. Piwowarczyk, F. Pointurier, Contribution to the development of atmospheric radioxenon monitoring, Journal of Radioanalytical and Nuclear Chemistry. 276 (2008) 391–398. https://doi.org/10.1007/s10967-008-0517-x.

[19] G. Le Petit, A. Cagniant, P. Gross, G. Douysset, S. Topin, J.P. Fontaine, T. Taffary, C. Moulin, Spalax™ new generation: A sensitive and selective noble gas system for nuclear explosion monitoring, Applied Radiation and Isotopes. 103 (2015) 102–114. https://doi.org/10.1016/j.apradiso.2015.05.019.

[20] A. Becker, G. Wotawa, A. Ringbom, P.R.J. Saey, Backtracking of Noble Gas Measurements Taken in the Aftermath of the Announced October 2006 Event in North Korea by Means of PTS Methods in Nuclear Source Estimation and Reconstruction, Pure and Applied Geophysics. 167 (2010) 581–599. https://doi.org/10.1007/s00024-009-0025-0.

[21] B. Orr, M. Schöppner, R. Tinker, W. Plastino, Detection of radioxenon in Darwin, Australia following the Fukushima Dai-ichi nuclear power plant accident, Journal of Environmental Radioactivity. 126 (2013) 40–44. https://doi.org/10.1016/j.jenvrad.2013.07.002.

[22] W. Shilian, L. Qi, M. Qinghua, C. Zhanying, Z. Yungang, L. Huijuan, J. Huaimao, C. Yinzhong, L. Shujiang, Z. Xinjun, F. Yuanqing, W. Ling, L. Yun, Radioxenon monitoring in Beijing following the Fukushima Daiichi NPP accident, Applied Radiation and Isotopes. 81 (2013) 344–347. https://doi.org/10.1016/j.apradiso.2013.03.049.

[23] P.R.J. Saey, M. Bean, A. Becker, J. Coyne, R. d'Amours, L.-E. De Geer, R. Hogue, T.J. Stocki, R.K. Ungar, G. Wotawa, A long-distance measurement of radioxenon in Yellowknife, Canada, in late October 2006, Geophysical Research Letters. 34 (2007). https://doi.org/10.1029/2007GL030611.

[24] A. Ringbom, A. Axelsson, M. Aldener, M. Auer, T.W. Bowyer, T. Fritioff, I. Hoffman, K. Khrustalev, M. Nikkinen, V. Popov, Y. Popov, K. Ungar, G. Wotawa, Radioxenon detections in the CTBT international monitoring system likely related to the announced nuclear test in North Korea on February 12, 2013, Journal of Environmental Radioactivity. 128 (2014) 47–63. https://doi.org/10.1016/j.jenvrad.2013.10.027.

[25] A. Ringbom, K. Elmgren, K. Lindh, J. Peterson, T.W. Bowyer, J.C. Hayes, J.I. McIntyre, M. Panisko, R. Williams, Measurements of radioxenon in ground level air in South Korea following the claimed nuclear test in North Korea on October 9, 2006, Journal of Radioanalytical and Nuclear Chemistry. 282 (2009) 773–779. https://doi.org/10.1007/s10967-009-0271-8.

[26] T.W. Bowyer, S.R. Biegalski, M. Cooper, P.W. Eslinger, D. Haas, J.C. Hayes, H.S. Miley, D.J. Strom, V. Woods, Elevated radioxenon detected remotely following the Fukushima nuclear accident, Journal of Environmental Radioactivity. 102 (2011) 681–687. https://doi.org/10.1016/j.jenvrad.2011.04.009.

[27] F. Xie, X. He, W. Jiang, X. Zhang, Q. Shi, S. Wu, L. Liu, C. Zhang, L. Chen, Development of a radioxenon measurement system and its application in monitoring Fukushima nuclear accident, Radiation Physics and Chemistry. 97 (2014) 85–89. https://doi.org/10.1016/j.radphyschem.2013.11.011.

[28] V. Doost-Mohammadi, H. Afarideh, G.R. Etaati, M.J. Safari, H. Rouhi, INGAS: Iranian Noble Gas Analyzing System for radioxenon measurement, Radiation Physics and Chemistry. 120 (2016) 26–32. https://doi.org/10.1016/j.radphyschem.2015.10.020.

[29] C.E. Cox, W. Hennig, A.C. Huber, W.K. Warburton, P.M. Grudberg, S.J. Asztalos, H. Tan, S. Biegalski, A 24-element Silicon PIN diode detector for high resolution radioxenon measurements using simultaneous X-ray and electron spectroscopy, in: 2013 IEEE Nuclear Science Symposium and Medical Imaging Conference (2013 NSS/MIC), IEEE, Seoul, Korea (South), 2013: pp. 1–7. https://doi.org/10.1109/NSSMIC.2013.6829481.

[30] W. Hennig, W.K. Warburton, A. Fallu-Labruyere, K. Sabourov, M.W. Cooper, J.I. McIntyre, A. Gleyzer, M. Bean, E.P. Korpach, K. Ungar, W. Zhang, P. Mekarski, Development of a phoswich detector system for radioxenon monitoring, Journal of Radioanalytical and Nuclear Chemistry. 282 (2009) 681–685. https://doi.org/10.1007/s10967-009-0181-9.

[31] F. Xie, W. Jiang, X. Li, X. He, J. Zhang, G. Yu, Single channel beta–gamma coincidence system for radioxenon measurement using well-type HPGe and plastic scintillator detectors, Nuclear Instruments and Methods in Physics Research Section A: Accelerators, Spectrometers, Detectors and Associated Equipment. 729 (2013) 900–904. https://doi.org/10.1016/j.nima.2013.08.070.

[32] B. Alemayehu, A.T. Farsoni, L. Ranjbar, E.M. Becker, A well-type phoswich detector for nuclear explosion monitoring, Journal of Radioanalytical and Nuclear Chemistry. 301 (2014) 323–332. https://doi.org/10.1007/s10967-014-3182-2.

[33] J.H. Ely, C.E. Aalseth, J.I. McIntyre, Novel beta-gamma coincidence measurements using phoswich detectors, Journal of Radioanalytical and Nuclear Chemistry. 263 (2005) 245–250. https://doi.org/10.1007/s10967-005-0044-y.

[34] C.B. Sivels, J.I. McIntyre, A.M. Prinke, A.R. Day, C. Lynch, S.D. Clarke, S.A. Pozzi, Stilbene cell development to improve radioxenon detection, Nuclear Instruments and Methods in Physics Research Section A: Accelerators, Spectrometers, Detectors and Associated Equipment. 923 (2019) 72–78. https://doi.org/10.1016/j.nima.2019.01.022.

[35] C.B. Sivels, J.I. McIntyre, T.W. Bowyer, M.B. Kalinowski, S.A. Pozzi, A review of the developments of radioxenon detectors for nuclear explosion monitoring, Journal of Radioanalytical and Nuclear Chemistry. 314 (2017) 829–841. https://doi.org/10.1007/s10967-017-5489-2.

[36] L. Bläckberg, T. Fritioff, L. Mårtensson, F. Nielsen, A. Ringbom, H. Sjöstrand, M. Klintenberg, Memory effect, resolution, and efficiency measurements of an Al2O3 coated plastic scintillator used for radioxenon detection, Nuclear Instruments and Methods in Physics Research Section A: Accelerators, Spectrometers, Detectors and Associated Equipment. 714 (2013) 128–135. https://doi.org/10.1016/j.nima.2013.02.045.

[37] W. Hennig, C.E. Cox, S.J. Asztalos, H. Tan, P.J. Franz, P.M. Grudberg, W.K. Warburton, A. Huber, Study of silicon detectors for high resolution radioxenon measurements, Journal of Radioanalytical and Nuclear Chemistry. 296 (2013) 675–681. https://doi.org/10.1007/s10967-012-2053-y.

[38] L. Bläckberg, A. Fay, I. Jõgi, S. Biegalski, M. Boman, K. Elmgren, T. Fritioff, A. Johansson, L. Mårtensson, F. Nielsen, A. Ringbom, M. Rooth, H. Sjöstrand, M. Klintenberg, Investigations of surface coatings to reduce memory effect in plastic scintillator detectors used for radioxenon detection, Nuclear Instruments and Methods in Physics Research Section A: Accelerators, Spectrometers, Detectors and Associated Equipment. 656 (2011) 84–91. https://doi.org/10.1016/j.nima.2011.07.038.

[39] L. Ranjbar, A.T. Farsoni, E.M. Becker, 135 Xe measurements with a two-element CZT-based radioxenon detector for nuclear explosion monitoring, Journal of Environmental Radioactivity. 169–170 (2017) 221–228. https://doi.org/10.1016/j.jenvrad.2016.12.003.

[40] L. Ranjbar, A.T. Farsoni, E.M. Becker, A CZT-based radioxenon detection system in support of the Comprehensive Nuclear-Test-Ban Treaty, Journal of Radioanalytical and Nuclear Chemistry. 310 (2016) 969–978. https://doi.org/10.1007/s10967-016-4872-8.

[41] S.A. Czyz, A.T. Farsoni, A radioxenon detection system using CdZnTe, an array of SiPMs, and a plastic scintillator, Journal of Radioanalytical and Nuclear Chemistry. 313 (2017) 131–140. https://doi.org/10.1007/s10967-017-5287-x.

[42] S.A. Czyz, A.T. Farsoni, L. Ranjbar, A prototype detection system for atmospheric monitoring of xenon radioisotopes, Nuclear Instruments and Methods in Physics Research Section A: Accelerators, Spectrometers, Detectors and Associated Equipment. 884 (2018) 64–69. https://doi.org/10.1016/j.nima.2017.10.044.

[43] H.R. Gadey, A.T. Farsoni, S.A. Czyz, K.D. McGee, A stilbene - CdZnTe based radioxenon detection system, Journal of Environmental Radioactivity. 204 (2019) 117–124. https://doi.org/10.1016/j.jenvrad.2019.03.027.

[44] H.R. Gadey, Abi T. Farsoni, S.A. Czyz, Preliminary results from a Stilbene-CdZnTe based Radioxenon Detection System, (2018). https://doi.org/10.13140/RG.2.2.12612.88963.

[45] H.R. Gadey, Abi T. Farsoni, S.A. Czyz, N. Shaheen, CdZnTe and Stilbene based radioxenon detection system, (2018). https://doi.org/10.13140/RG.2.2.19323.77608.

[46] S.A. Czyz, A.T. Farsoni, H.R. Gadey, Evaluation of a semiconductor-based atmospheric radioxenon detection system, Nuclear Instruments and Methods in Physics Research Section A: Accelerators, Spectrometers, Detectors and Associated Equipment. 945 (2019) 162614. https://doi.org/10.1016/j.nima.2019.162614.

[47] S.A. Czyz, A.M. Alhawsawi, A.T. Farsoni, H.R. Gadey, L. Ranjbar, M.A. Mannino, K.D. McGee, A radioxenon detection system using PIPS and CZT, Journal of Radioanalytical and Nuclear Chemistry. (2018). https://doi.org/10.1007/s10967-018-6367-2.

[48] S.A. Czyz, Abi.T. Farsoni, H.R. Gadey, A PIPS + SrI2(Eu) detector for atmospheric radioxenon monitoring, Nuclear Instruments and Methods in Physics Research Section A: Accelerators, Spectrometers, Detectors and Associated Equipment. 1012 (2021) 165619. https://doi.org/10.1016/j.nima.2021.165619.

[49] SensL, Array J User Manual. https://sensl.com/downloads/ds/UM-ArrayTSV.pdf [Accessed: 7 Sep 2021]

[50] E. Becker, M. Mannino, A. Farsoni, C.-S. Lee, Eight-Channel Digital Spectrometer for Coincidence Measurements in Multi-element Detectors, (2016). http://cvt.engin.umich.edu/wp-content/uploads/sites/173/2016/07/Poster25-becker-2016_cvt_r2.1.pdf. [Accessed: 7 Sep 2021]

[51] MathWorks, MATLAB. https://www.mathworks.com/products/matlab.html [Accessed: 7 Sep 2021]

[52] Inrad Optics Inc. https://www.inradoptics.com/ [Accessed: 7 Sep 2021]

[53] CapeSym Inc. https://www.capesym.com/ [Accessed: 7 Sep 2021]

[54] Analog Devices, LT8410/LT8410-1. https://www.analog.com/media/en/technical-documentation/data-sheets/84101fc.pdf [Accessed: 7 Sep 2021]

[55] Cremat Inc., CR-113-R2.1 charge sensitive preamplifier: application guide. https://www.cremat.com/CR-113-R2.1.pdf [Accessed: 7 Sep 2021]

[56] Opal Kelly. https://opalkelly.com/ [Accessed: 7 Sep 2021]

[57] Xilinx, Kintex-7. https://www.xilinx.com/products/silicon-devices/fpga/kintex-7.html [Accessed: 7 Sep 2021]

[58] H.R. Gadey, Development of a Radioxenon Detection System using Stilbene and Strontium Iodide, Oregon State University, n.d. https://ir.library.oregonstate.edu/concern/graduate_thesis_or_dissertations/44558n148. [Accessed: 7 Sep 2021]

[59] M.W. Cooper, J.H. Ely, D.A. Haas, J.C. Hayes, J.I. McIntyre, L.S. Lidey, B.T. Schrom, Absolute Efficiency Calibration of a Beta-Gamma Detector, IEEE Trans. Nucl. Sci. 60 (2013) 676–680. https://doi.org/10.1109/TNS.2013.2243165.

[60] W.K. Warburton, W. Hennig, J.A. Bertrand, S.M. George, S. Biegalski, Atomic layer deposition α-Al2O3 diffusion barriers to eliminate the memory effect in beta-gamma radioxenon detectors, J Radioanal Nucl Chem. 296 (2013) 541–549. https://doi.org/10.1007/s10967-012-2061-y.

[61] M.W. Cooper, J.C. Hayes, B.T. Schrom, J.H. Ely, J.I. McIntyre, Minimum Detectable Concentration and Concentration Calculations, 2016. https://doi.org/10.2172/1526738.

[62] J.C. Hayes, M.W. Cooper, M.A. Covert, J.H. Ely, M.P. Foxe, D.A. Haas, W.W. Harper, T.R. Heimbigner, C.W. Hubbard, D.T. Keller, P.H. Humble, J.C. Madison, S.J. Morris, M.E. Panisko, A.M. Prinke, M.D. Ripplinger, T.L. Stewart, Requirements for Xenon International: Revision 1, Pacific Northwest National Laboratory (PNNL), Richland, WA (US), 2015. https://www.pnnl.gov/main/publications/external/technical_reports/PNNL-22227Rev1.pdf. [Accessed: 7 Sep 2021]

[63] J.C. Hayes, M.W. Cooper, M.A. Covert, J. Ely, M.P. Foxe, D.A. Haas, W.W. Harper, T.R. Heimbigner, C.W. Hubbard, D.T. Keller, P.H. Humble, J.C. Madison, S.J. Morris, M.E. Panisko, A.M. Prinke, M.D. Ripplinger, T.L. Stewart, Requirements for Xenon International (Rev. 2), 2018. https://doi.org/10.2172/1545382.

[64] J.C. Hayes, W. Harper, M. Panisko, M.W. Cooper, Xenon International Overview, 2018. https://doi.org/10.2172/1472068.

[65] Comprehensive Nuclear-Test-Ban Treaty Organization, Conferences Trainings & Workshops. https://ctnw.ctbto.org/DMZ/event/3239/posters/F22C0FB597434C9DB3874D8FECF253FB [Accessed: 7 Sep 2021]